A&A 596, A110 (2016)
DOI: 10.1051/0004-6361/201629018

Astronomy & Astrophysics

Planck intermediate results

XLIX. Parity-violation constraints from polarization data

Planck Collaboration: N. Aghanim[47], M. Ashdown[57,4], J. Aumont[47], C. Baccigalupi[67], M. Ballardini[23,38,41], A. J. Banday[77,7], R. B. Barreiro[52], N. Bartolo[22,53], S. Basak[67], K. Benabed[48,76], J.-P. Bernard[77,7], M. Bersanelli[26,39], P. Bielewicz[65,7,67], L. Bonavera[12], J. R. Bond[6], J. Borrill[9,73], F. R. Bouchet[48,72], C. Burigana[38,24,41], E. Calabrese[74], J.-F. Cardoso[60,1,48], J. Carron[17], H. C. Chiang[19,5], L. P. L. Colombo[15,54], B. Comis[61], D. Contreras[14], F. Couchot[58], A. Coulais[59], B. P. Crill[54,8], A. Curto[52,4,57], F. Cuttaia[38], P. de Bernardis[25], A. de Rosa[38], G. de Zotti[35,67], J. Delabrouille[1], F.-X. Désert[45], E. Di Valentino[48,72], C. Dickinson[55], J. M. Diego[52], O. Doré[54,8], A. Ducout[48,46], X. Dupac[30], S. Dusini[53], F. Elsner[16,48,76], T. A. Enßlin[63], H. K. Eriksen[50], Y. Fantaye[29], F. Finelli[38,41], F. Forastieri[24,42], M. Frailis[37], E. Franceschi[38], A. Frolov[71], S. Galeotta[37], S. Galli[56], K. Ganga[1], R. T. Génova-Santos[51,11], M. Gerbino[75,66,25], Y. Giraud-Héraud[1], J. González-Nuevo[12,52], K. M. Górski[54,79], A. Gruppuso[38,41,⋆], J. E. Gudmundsson[75,66,19], F. K. Hansen[50], S. Henrot-Versillé[58], D. Herranz[52], E. Hivon[48,76], Z. Huang[6], A. H. Jaffe[46], W. C. Jones[19], E. Keihänen[18], R. Keskitalo[9], K. Kiiveri[18,34], N. Krachmalnicoff[26], M. Kunz[10,47,2], H. Kurki-Suonio[18,34], J.-M. Lamarre[59], M. Langer[47], A. Lasenby[4,57], M. Lattanzi[24,42], C. R. Lawrence[54], M. Le Jeune[1], J. P. Leahy[55], F. Levrier[59], M. Liguori[22,53], P. B. Lilje[50], V. Lindholm[18,34], M. López-Caniego[30], Y.-Z. Ma[55,68], J. F. Macías-Pérez[61], G. Maggio[37], D. Maino[26,39], N. Mandolesi[38,24], M. Maris[37], P. G. Martin[6], E. Martínez-González[52], S. Matarrese[22,53,32], N. Mauri[41], J. D. McEwen[64], P. R. Meinhold[20], A. Melchiorri[25,43], A. Mennella[26,39], M. Migliaccio[49,57], M.-A. Miville-Deschênes[47,6], D. Molinari[24,38,42], A. Moneti[48], G. Morgante[38], A. Moss[70], P. Natoli[24,3,42], L. Pagano[25,43], D. Paoletti[38,41], G. Patanchon[1], L. Patrizii[41], L. Perotto[61], V. Pettorino[33], F. Piacentini[25], L. Polastri[24,42], G. Polenta[3,36], J. P. Rachen[13,63], B. Racine[1], M. Reinecke[63], M. Remazeilles[55,47,1], A. Renzi[29,44], G. Rocha[54,8], C. Rosset[1], M. Rossetti[26,39], G. Roudier[1,59,54], J. A. Rubiño-Martín[51,11], B. Ruiz-Granados[78], M. Sandri[38], M. Savelainen[18,34], D. Scott[14], C. Sirignano[22,53], G. Sirri[41], L. D. Spencer[69], A.-S. Suur-Uski[18,34], J. A. Tauber[31], D. Tavagnacco[37,27], M. Tenti[40], L. Toffolatti[12,52,38], M. Tomasi[26,39], M. Tristram[58], T. Trombetti[38,24], J. Valiviita[18,34], F. Van Tent[62], P. Vielva[52], F. Villa[38], N. Vittorio[28], B. D. Wandelt[48,76,21], I. K. Wehus[54,50], A. Zacchei[37], and A. Zonca[20]

(Affiliations can be found after the references)

Received 27 May 2016 / Accepted 4 August 2016

ABSTRACT

Parity-violating extensions of the standard electromagnetic theory cause in vacuo rotation of the plane of polarization of propagating photons. This effect, also known as cosmic birefringence, has an impact on the cosmic microwave background (CMB) anisotropy angular power spectra, producing non-vanishing T–B and E–B correlations that are otherwise null when parity is a symmetry. Here we present new constraints on an isotropic rotation, parametrized by the angle α, derived from *Planck* 2015 CMB polarization data. To increase the robustness of our analyses, we employ two complementary approaches, in harmonic space and in map space, the latter based on a peak stacking technique. The two approaches provide estimates for α that are in agreement within statistical uncertainties and are very stable against several consistency tests. Considering the T–B and E–B information jointly, we find $\alpha = 0.^\circ31 \pm 0.^\circ05$ (stat.) $\pm 0.^\circ28$ (syst.) from the harmonic analysis and $\alpha = 0.^\circ35 \pm 0.^\circ05$ (stat.) $\pm 0.^\circ28$ (syst.) from the stacking approach. These constraints are compatible with no parity violation and are dominated by the systematic uncertainty in the orientation of *Planck*'s polarization-sensitive bolometers.

Key words. cosmology: observations – cosmic background radiation – cosmological parameters – methods: data analysis – methods: statistical

1. Introduction

Measuring the in vacuo rotation of the plane of polarization of photons is a way to test fundamental physics in the Universe. Such a rotation is sensitive to parity-violating interactions in the electromagnetic sector that are found in extensions of the Standard Model of particle physics (Carroll 1998; Lue et al. 1999; Feng et al. 2005; Li et al. 2009). For example, extending the Maxwell Lagrangian with a coupling (scalar, Chern-Simons, etc.) to $A_\nu \tilde{F}^{\mu\nu}$[1], impacts right- and left-handed photons asymmetrically. Therefore a photon at the last-scattering surface with linear polarization in one orientation will arrive at our detectors with its plane of polarization rotated due to this coupling term. The amount of rotation, usually denoted α, is often referred to as the cosmic birefringence angle. This rotation naturally mixes E- and B-modes of CMB polarization[2] and generates T–B and E–B correlations that would be zero in the absence of parity violations. The cosmic microwave background (CMB) polarization is particularly useful for measuring this effect because even if the coupling is small, CMB photons have travelled a large comoving distance from the last-scattering surface almost completely unimpeded and thus the rotation could accumulate into a measurable signal.

This effect has previously been investigated using data from many CMB experiments (Feng et al. 2006; Wu et al. 2009; Brown et al. 2009; Pagano et al. 2009; Komatsu et al. 2011; Hinshaw et al. 2013; Ade et al. 2014a,b; Kaufman et al. 2014; Naess et al. 2014; di Serego Alighieri et al. 2014; Zhao et al. 2015; Mei et al. 2015; Gruppuso et al. 2015; Contaldi 2015; Molinari et al. 2016), and also by looking at radio galaxy

⋆ Corresponding author: A. Gruppuso gruppuso@iasfbo.inaf.it

[1] Here A_ν is the photon field, and $\tilde{F}^{\mu\nu}$ is the dual of the Faraday tensor, defined to be $\tilde{F}^{\mu\nu} \equiv (1/2)\epsilon^{\mu\nu\rho\sigma}F_{\rho\sigma}$.

[2] We use the customary convention used by the CMB community for the Q and U Stokes parameters, see, e.g., http://wiki.cosmos.esa.int/planckpla2015/index.php/Sky_temperature_maps

data (Carroll et al. 1990; Cimatti et al. 1993, 1994; Wardle et al. 1997; Leahy 1997; Carroll 1998; di Serego Alighieri et al. 2010; Kamionkowski 2010). Thus far all the constraints are compatible with no cosmic birefringence (see discussion in Sect. 7).

In this paper we employ *Planck*[3] 2015 CMB data to estimate an isotropic α. The birefringence angle has already been constrained with *Planck* data in Gruppuso et al. (2015), using the publicly available 2015 *Planck* Likelihood (Planck Collaboration XI 2016). However, that work did not use T–B and E–B data, which are essential for determining the sign of α and for increasing the constraining power. We include here T–B and E–B cross-correlations by considering two approaches, one based on harmonic space through the use of the so-called D-estimators and one based on pixel-space maps that employs stacked images of the transformed $Q_{\rm r}$ and $U_{\rm r}$ Stokes parameters.

The paper is organized as follows. In Sect. 2 we describe the effect that cosmological birefringence has on the angular power spectra of the CMB. In Sect. 3 we provide details of the data and simulations that are considered in our analysis, which is described in Sect. 4. Results for our two different methodologies are summarized and compared in Sect. 5. Section 6 contains a discussion of the systematic effects that are most important for the observables considered. Finally, conclusions are drawn in Sect. 7.

2. Impact of birefringence on the CMB polarization spectra

Birefringence rotates the six CMB angular power spectra in the following way (see Lue et al. 1999; Feng et al. 2006, for more details):

$$C'^{TT}_\ell = C^{TT}_\ell; \tag{1}$$

$$C'^{EE}_\ell = C^{EE}_\ell \cos^2(2\alpha) + C^{BB}_\ell \sin^2(2\alpha); \tag{2}$$

$$C'^{BB}_\ell = C^{EE}_\ell \sin^2(2\alpha) + C^{BB}_\ell \cos^2(2\alpha); \tag{3}$$

$$C'^{TE}_\ell = C^{TE}_\ell \cos(2\alpha); \tag{4}$$

$$C'^{TB}_\ell = C^{TE}_\ell \sin(2\alpha); \tag{5}$$

$$C'^{EB}_\ell = \frac{1}{2}\left(C^{EE}_\ell - C^{BB}_\ell\right)\sin(4\alpha). \tag{6}$$

Here α is assumed to be constant (see Liu et al. 2006; Finelli & Galaverni 2009; Li & Zhang 2008 for generalizations). In this paper we will consider only the above parametrization, where the primed C'_ℓ are the observed spectra and the unprimed C_ℓ are the spectra one would measure in the absence of parity violations. In principle the rotation angle α could depend on direction (with details dictated by the specific model considered), and one could measure the anisotropies of α. We do not employ this type of analysis here, but focus on the simple case of an *isotropic* α (or the α monopole; see Gluscevic et al. 2012 and Ade et al. 2015 for constraints on anisotropic birefringence).

Isotropic birefringence is indistinguishable from a systematic, unknown mismatch of the global orientation of the polarimeters. This is strictly true if the cosmological birefringence α is the same regardless of the multipole ℓ at which CMB polarization is measured. However, specific birefringence models may predict some angular dependence in α. Furthermore, large angular scale polarization in α is sourced in the re-ionization epoch, as opposed to the small scales which are formed at recombination (Komatsu et al. 2011; Gruppuso et al. 2015). This will inevitably produce some angular dependency in α (assuming that the birefringence angle is proportional to the CMB photon path) and this effect could in principle be used to disentangle instrumental systematic effects (since photons that scattered at the re-ionization epoch would have traveled less than the others). However, we focus here on smaller scale data, where the reionization effects are not important and therefore such a distinction is not possible. For *Planck* there is an estimate of the uncertainty of the possible instrument polarization angle using measurements performed on the ground (Rosset et al. 2010), as discussed further in Sect. 6. Unfortunately, in-flight calibration is complicated by the scarcity of linearly polarized sources that are bright enough, with the Crab Nebula being a primary calibration source (Planck Collaboration VIII 2016)[4].

Equations (1)–(6) include all the secondary anisotropies but the weak-lensing effect. Due the current precision of data (see the discussion in Gubitosi et al. 2014) we safely ignore the weak-lensing effect as it contributes a negligible error.

3. Data and simulations

We use the full-mission *Planck* (Planck Collaboration I 2016) component-separated temperature and high-pass-filtered polarization maps at `HEALPix`[5] (Górski et al. 2005) resolution $N_{\rm side} = 1024$; i.e., we take the `Commander`, `NILC`, `SEVEM`, and `SMICA` solutions for T, Q, U, and E, fully described in Planck Collaboration IX (2016) and Planck Collaboration X (2016), and available on the Planck Legacy Archive[6]. The E-mode maps are calculated using the method of Bielewicz et al. (2012; see also Kim 2011). We use the common temperature and polarization masks at $N_{\rm side} = 1024$, namely $\mathtt{UT}_{1024}\mathtt{76}$ and `UPB77`, respectively. For the harmonic analysis we also use half-mission data provided by the `SMICA` component-separation pipeline, in order to build our D^{EB}-estimator from cross-correlations (Planck Collaboration IX 2016). No further smoothing is applied to any of the maps (although this version of the data already includes 10′ smoothing in both temperature and polarization).

We note that there are known systematic effects in the polarization maps released by *Planck* that have not been fully remedied in the 2015 release (see Sect. 6 for a full discussion on the main systematic effects relevant for this analysis). These issues include various sources of large angular scale artefacts, temperature-to-polarization leakage (Planck Collaboration VII 2016; Planck Collaboration VIII 2016; Planck Collaboration XI 2016), and a mismatch in noise properties between the data and simulations (Planck Collaboration XII 2016). In order to mitigate any large-angle artefacts, we use only the high-pass-filtered version of the polarization data. We note that neglecting the large scales has little to no impact on our constraining power for α. We have also checked that temperature-to-polarization leakage (Planck Collaboration XI 2016) has very little effect on our analysis (see Sect. 6.2); similar conclusions are reached in Planck Collaboration XLVI (2016).

[3] *Planck* (`http://www.esa.int/Planck`) is a project of the European Space Agency (ESA) with instruments provided by two scientific consortia funded by ESA member states and led by Principal Investigators from France and Italy, telescope reflectors provided through a collaboration between ESA and a scientific consortium led and funded by Denmark, and additional contributions from NASA (USA).

[4] We do not employ any self-calibration procedure as suggested in Keating et al. (2012) since it is degenerate with the effect we are looking for.

[5] `http://healpix.sourceforge.net/`

[6] `http://www.cosmos.esa.int/web/planck/pla`

We pay particular attention to the mis-characterization of the noise in the polarization data. Given the recommendation in Planck Collaboration IX (2016) we restrict our analysis to cross-correlation and stacking methods, which are less sensitive to such noise issues (Planck Collaboration VIII 2016). For the harmonic analysis, we estimate the angular power spectra up to multipoles $\ell \simeq 1500$ (as suggested by the cosmological analysis tests carried out in Planck Collaboration IX 2016), using simulations to create a χ^2 statistic. The map-space analysis does not require the use of simulations[7], since we only need a relatively crude noise estimate on the scales we work at and we use a weighting approach when stacking that is only dependent on the data (we have also checked that our results are quite insensitive to the noise level of the data, see Sect. 6.1). Nevertheless it is reassuring that the map-space and harmonic-space analyses arrive at consistent results.

We use realistic full focal plane (FFP8.1) simulations described in detail in Planck Collaboration XII (2016). These are 10^3 simulations processed through the four *Planck* component-separation pipelines, namely `Commander`, `NILC`, `SEVEM`, and `SMICA` (Planck Collaboration IX 2016), using the same weights as derived from the *Planck* full mission data. The CMB output maps are used to build the harmonic space estimators used in this work. For our harmonic space EB estimator we use the half-mission simulations provided by the `SMICA` pipeline.

The FFP8.1 fiducial cosmology corresponds to the cosmological parameters $\omega_\mathrm{b} = 0.0222$, $\omega_\mathrm{c} = 0.1203$, $\omega_\nu = 0.00064$, $\Omega_\Lambda = 0.6823$, $h = 0.6712$, $n_\mathrm{s} = 0.96$, $A_\mathrm{s} = 2.09 \times 10^{-9}$, and $\tau = 0.065$ (where $\omega_\mathrm{x} \equiv \Omega_\mathrm{x} h^2$). We note that we perform the analysis for the birefringence angle by fixing the other cosmological parameters to the values reported above. This seems to be a safe assumption, since in Gruppuso et al. (2015) it was shown that α is quite decoupled from the other parameters, at least as long as C_ℓ^{TT}, C_ℓ^{TE}, and C_ℓ^{EE} are considered; ΛCDM parameters are not expected to be constrainted much from C_ℓ^{TB} and C_ℓ^{EB}, contrary to models that explicitly break parity symmetry.

4. Analysis

4.1. Map-space analysis

We follow the stacking approach first introduced in Komatsu et al. (2011), where they were able to constrain α by stacking polarization on temperature extrema. Here we perform the same analysis, but also stack on E-mode extrema. Our analysis is performed in map space (although we must briefly go to harmonic space for stacking on E-modes, as described in Sect. 6.1) and we show that stacking polarization on temperature extrema is sensitive to the T–E and T–B correlations, while stacking on E-mode extrema is sensitive to the E–E and E–B correlations.

The recommendation on the use of polarization data from Planck Collaboration IX (2016) is that only results with weak dependence on noise are to be considered completely reliable. For the purposes of stacking on temperature peaks only cross-correlation information is used, and thus understanding the detailed noise properties of polarization is unnecessary. Stacking on E-mode peaks the results *do* depend on the noise properties of the map; this is because the expected angular profiles of the stacks depend on the full power spectrum of the map. In Sect. 6.1 we demonstrate that even a strong miscalculation of the noise would result in shifts at below the 1σ level (and more reasonable miscalculations of the noise will bias results at an essentially negligible level).

4.1.1. Q_r and U_r parameters

We use the transformed Stokes parameters Q_r, and U_r, first introduced in Kamionkowski et al. (1997):

$$Q_\mathrm{r}(\boldsymbol{\theta}) = -Q(\boldsymbol{\theta})\cos(2\phi) - U(\boldsymbol{\theta})\sin(2\phi); \tag{7}$$

$$U_\mathrm{r}(\boldsymbol{\theta}) = Q(\boldsymbol{\theta})\sin(2\phi) - U(\boldsymbol{\theta})\cos(2\phi). \tag{8}$$

Here ϕ is defined as the angle from a local east (where north always points towards the Galactic north pole) direction in the coordinate system defined by centring on the hot or cold spot, and $\boldsymbol{\theta}$ is a radial vector. The stacking procedure tends to produce images with azimuthal symmetry, and hence the predictions will only depend on θ. The theoretical angular profiles for stacking on temperature hot spots are derived in Komatsu et al. (2011, see also Planck Collaboration XVI 2016) and are explicitly given by

$$\left\langle Q_\mathrm{r}^T \right\rangle(\theta) = -\int \frac{\ell \mathrm{d}\ell}{2\pi} W_\ell^T W_\ell^P \left(\bar{b}_\nu + \bar{b}_\zeta \ell^2\right) C_\ell^{TE} J_2(\ell\theta), \tag{9}$$

$$\left\langle U_\mathrm{r}^T \right\rangle(\theta) = -\int \frac{\ell \mathrm{d}\ell}{2\pi} W_\ell^T W_\ell^P \left(\bar{b}_\nu + \bar{b}_\zeta \ell^2\right) C_\ell^{TB} J_2(\ell\theta). \tag{10}$$

The quantities $W_\ell^{T,P}$ are combinations of the beam (10′ smoothing) and pixel window functions (at $N_\mathrm{side} = 1024$) for temperature and polarization. Below we will use W_ℓ^E to denote the same quantity for E-modes; however, the E-modes are produced at the same resolution as temperature and so $W_\ell^E = W_\ell^T$. The bracketed term in each of Eqs. (9) and (10) incorporates the scale-dependent bias when converting the underlying density field to temperature or E-modes (thus, they will differ if the stacking is performed on temperature or E-mode extrema). The function J_2 is the second-order Bessel function of the first kind. Angular profiles derived from stacking on E-mode hot spots can easily be generalized from the above formulae by simply noting that E-modes share the same statistical properties as temperature and thus we only need to change the power spectra in the above formulae. Thus the angular profiles for stacking on E-mode hot spots are given by

$$\left\langle Q_\mathrm{r}^E \right\rangle(\theta) = -\int \frac{\ell \mathrm{d}\ell}{2\pi} W_\ell^E W_\ell^P \left(\bar{b}_\nu + \bar{b}_\zeta \ell^2\right) \left(C_\ell^{EE} + N_\ell^{EE}\right) J_2(\ell\theta), \tag{11}$$

$$\left\langle U_\mathrm{r}^E \right\rangle(\theta) = -\int \frac{\ell \mathrm{d}\ell}{2\pi} W_\ell^E W_\ell^P \left(\bar{b}_\nu + \bar{b}_\zeta \ell^2\right) C_\ell^{EB} J_2(\ell\theta). \tag{12}$$

The specific forms of b_ν (the scale-independent part) and b_ζ (which is proportional to second derivatives that define the peak) are given in Desjacques (2008). The ΛCDM prediction for $\left\langle U_\mathrm{r}^{T,E} \right\rangle$ is identically zero and thus we will find that the vast majority of the constraining power comes from these profiles. We also show explicitly in Eqs. (9)–(12) that Q_r and U_r are sensitive to the T–E and T–B correlation when stacking on temperature extrema or the E–E and E–B correlation when stacking on E-mode extrema. Determination of the bias parameters depends on the power spectrum of the map where the extrema are determined (see Komatsu et al. 2011, and Appendix A), thus they depend on the noise properties of the map, as well as the underlying power spectrum. Section 6.1 will examine to what extent misunderstanding the noise might bias the results.

[7] We explicitly checked that using simulations does not change the results, which is simply a consequence of the fact that the process of stacking means we are not very sensitive to the noise properties of the data.

For our main results we have selected extrema using a threshold of $\nu = 0$, which mean we consider *all* positive hot spots (or negative cold spots); however, we have checked other choices of threshold and found consistency, provided that we do not choose such a high a threshold such that the overall signal becomes too weak. We do not claim that our analysis is optimal, and it may be that a better weighting exists for different levels of threshold; however, tests have shown that, in terms of minimizing the uncertainty on α, the choice of $\nu = 0$ and use of averaged bias parameters is close to optimal.

For the *Planck* temperature data we calculate the bias parameters to be $\bar{b}_\nu = 3.829 \times 10^{-3}\ \mu\mathrm{K}^{-1}$ and $\bar{b}_\zeta = 1.049 \times 10^{-7}\ \mu\mathrm{K}^{-1}$. For the *Planck* E-mode data we calculate $\bar{b}_\nu = (3.622, 3.384, 2.957, 3.332) \times 10^{-2}\ \mu\mathrm{K}^{-1}$ and $\bar{b}_\zeta = (1.727, 3.036, 1.874, 3.039) \times 10^{-7}\ \mu\mathrm{K}^{-1}$ for `Commander`, `NILC`, `SEVEM`, and `SMICA`, respectively. The derivation of Eqs. (9)–(10) and a discussion of how to calculate all relevant quantities are given in Appendix B of Komatsu et al. (2011), while the derivation of Eqs. (11)–(12) is given in Appendix A of this paper. The reader is referred to Komatsu et al. (2011) and also Sect. 8 of of Planck Collaboration XVI (2016) for a complete description of the physics behind the features in the predicted stacked profiles.

4.1.2. Procedure

We begin by locating all local extrema[8] of the temperature (or E-mode) data outside the region defined by the mask, i.e., either the union of temperature and polarization common masks for stacking on temperature extrema or simply the polarization common masks when stacking on E-mode extrema. These masks remove the Galactic plane, as well as the brighter point sources. We define a $5^\circ \times 5^\circ$ grid, with the size of each pixel being $0.^\circ1$ and the number of pixels being 2500. When adding Q and U images, we weight each pixel by the number of unmasked $N_{\rm side} = 1024$ pixels that lie in each re-gridded pixel (which is not uniform, because of the re-gridding and masking; this weighting is used in the estimation of the covariance matrix of the stacked images). Therefore the pixels near the centre generally have somewhat lower noise in the final stacked image. We then generate $Q_{\rm r}^{T,E}$ and $U_{\rm r}^{T,E}$ images using Eqs. (7) and (8).

The predictions for $Q_{\rm r}$ and $U_{\rm r}$ are found by combining Eqs. (9)–(12) with Eqs. (2)–(6):

$$\left\langle Q_{\rm r}^T \right\rangle(\theta) = -\cos(2\alpha) \int \frac{\ell \mathrm{d}\ell}{2\pi} W_\ell^T W_\ell^P \left(\bar{b}_\nu + \bar{b}_\zeta \ell^2\right) C_\ell^{TE} J_2(\ell\theta); \quad (13)$$

$$\left\langle U_{\rm r}^T \right\rangle(\theta) = -\sin(2\alpha) \int \frac{\ell \mathrm{d}\ell}{2\pi} W_\ell^T W_\ell^P \left(\bar{b}_\nu + \bar{b}_\zeta \ell^2\right) C_\ell^{TE} J_2(\ell\theta). \quad (14)$$

For stacking on E-modes we have

$$\left\langle Q_{\rm r}^E \right\rangle(\theta) = -\int \frac{\ell \mathrm{d}\ell}{2\pi} W_\ell^E W_\ell^P \left(\bar{b}_\nu + \bar{b}_\zeta \ell^2\right) \left(C_\ell^{EE} \cos^2(2\alpha) + N_\ell^{EE}\right) J_2(\ell\theta), \quad (15)$$

$$\left\langle U_{\rm r}^E \right\rangle(\theta) = -\frac{1}{2}\sin(4\alpha) \int \frac{\ell \mathrm{d}\ell}{2\pi} W_\ell^E W_\ell^P \left(\bar{b}_\nu + \bar{b}_\zeta \ell^2\right) C_\ell^{EE} J_2(\ell\theta), \quad (16)$$

[8] As previously mentioned, we use *all* positive (negative) local maxima (minima) for hot (cold) spots. Extrema are defined by comparing each pixel to its nearest neighbours.

where we have assumed that $C_\ell^{BB} = 0$, which is consistent with our data since *Planck* does not have a direct detection of B-modes. We use a uniform prior on α, $P(\alpha)$, when sampling the likelihood, i.e.,

$$P(\alpha|d) \propto P(d|\alpha)P(\alpha), \quad (17)$$

with

$$P(d|\alpha) = \frac{1}{\sqrt{2\pi|\mathsf{C}|}} e^{-\frac{1}{2}\{d-(Q_{\rm r},U_{\rm r})(\alpha)\}^{\mathsf{T}}\mathsf{C}^{-1}\{d-(Q_{\rm r},U_{\rm r})(\alpha)\}}. \quad (18)$$

Here d represents the data, consisting of the stacked $Q_{\rm r}$ and $U_{\rm r}$ images, and $(Q_{\rm r}, U_{\rm r})(\alpha)$ are the predictions as a function of α (see Eqs. (13)–(16)). The quantity C is the covariance matrix, which is a combination of the noise in the data and the cosmic variance due to the limited number of hot (or cold) spots in the sky. We have estimated the covariance matrix by determining an rms level from the pixelization scheme chosen and then weighting this with the inverse of the total number of pixels used in each re-gridded pixel; we have also assumed that the covariance is diagonal in pixel space.

For the purposes of evaluating the likelihood, we have fixed C_ℓ^{TE} and C_ℓ^{EE} to the theoretical power spectra, based on the best-fit *Planck* parameters (Planck Collaboration XIII 2016), and simply evaluate the likelihood in a fine grid of α values. The choice of fixing the angular power spectra is reasonable because the usual cosmological parameters are determined by C_ℓ^{TT}, C_ℓ^{TE}, and C_ℓ^{EE}, which are minimally affected by α (no dependence, quadratic, and still quadratic dependence on α, respectively). See also comments at the end of Sect. 3.

Finally, we quote the mean of the posterior on α and the width of the posterior containing 68% of the likelihood as the best-fit and statistical uncertainty, respectively. The posterior for α is sufficiently Gaussian that these two values contain all necessary information about the posterior.

4.2. Harmonic-space analysis

The harmonic-based analysis uses the so-called D-estimators (see for instance Wu et al. 2009; Gruppuso et al. 2012, Zhao et al. 2015; Gruppuso et al. 2016), which are defined by the following equations:

$$D_\ell^{TB,\rm obs} = C_\ell'^{TB}\cos(2\hat{\alpha}) - C_\ell'^{TE}\sin(2\hat{\alpha}); \quad (19)$$

$$D_\ell^{EB,\rm obs} = C_\ell'^{EB}\cos(4\hat{\alpha}) - \frac{1}{2}(C_\ell'^{EE} - C_\ell'^{BB})\sin(4\hat{\alpha}). \quad (20)$$

Here $\hat{\alpha}$ is the estimate for the birefringence angle α. It is possible to show that on average

$$\langle D_\ell^{TB,\rm obs}\rangle = \langle C_\ell^{TE}\rangle \sin(2(\alpha - \hat{\alpha})), \quad (21)$$

$$\langle D_\ell^{EB,\rm obs}\rangle = \frac{1}{2}\left(\langle C_\ell^{EE}\rangle - \langle C_\ell^{BB}\rangle\right)\sin(4(\alpha - \hat{\alpha})). \quad (22)$$

Equations (21) and (22) are zero when

$$\hat{\alpha} = \alpha. \quad (23)$$

Equation (23) suggests that we can find α by looking for the $\hat{\alpha}$ that makes null the expectation values of the D-estimators. From now on we always consider that Eq. (23) is satisfied.

We estimate the angular power spectra using the `MASTER` method (Hivon et al. 2002) extended to polarization (Kogut et al. 2003; Polenta et al. 2005) to correct for masking, and we use simulations to estimate the noise. We choose a bin size of

$\Delta\ell = 20$, starting at $\ell_{\rm min} = 51$, to avoid correlations between bins induced by masking. It is then possible to minimize $\chi^2(\alpha)$ for TB and EB separately, or jointly to estimate α:

$$\chi^2_X(\alpha) = \sum_{bb'} D_b^{X,\rm obs} M^{XX^{-1}}_{bb'} D^{X,\rm obs}_{b'}, \tag{24}$$

where $X = TB$ or EB, b denotes the bin and $M^{XX}_{bb'} = \langle D^X_b D^X_{b'}\rangle$, where the average is taken over the FFP8.1 simulations described in Sect. 3 and generated with $\alpha = 0$. We thus are adopting a simple frequentist approach to test the null hypothesis of no parity violation. This approach also allows for the minimization of Eq. (24) in subintervals of multipoles, providing the possibility of searching for a possible angular scale dependence to the birefringence effect, i.e.,

$$\chi^2_X(\alpha) = \sum_b \chi^2_{X,b}(\alpha), \tag{25}$$

where $\chi^2_{X,b}(\alpha) = \sum_{b'} D_b^{X,\rm obs} M^{XX^{-1}}_{bb'} D^{X,\rm obs}_{b'}$. This will be used to test the stability of the estimates of α against the ranges of multipoles considered for the CMB spectra.

The D^{TB}-estimator is inherently built from cross-correlations (see Eq. (19)) and therefore we are able to use the full-mission data and simulations for all component-separation methods to generate the corresponding χ^2. Moreover, since the SMICA simulations are also delivered in half-mission form, we are additionally able to estimate D^{TB}_ℓ by cross-correlating half-mission 1 and half-mission 2 data and simulations.

Regarding the D^{EB}-estimator since it contains auto-correlations (see Eq. (20)), we must estimate it from the half-mission data along with simulations in order to satisfy the recommendations on the use of polarization data given in Planck Collaboration IX (2016), based on the fact that only results with a weak dependence on noise are to be considered fully reliable. More specifically, C'^{EE}_ℓ and C'^{BB}_ℓ are estimated from cross-correlating half-mission 1 with half-mission 2 SMICA data and using the corresponding SMICA simulations only.

5. Results

In the following subsections we present our constraints on α for the two methods, described in the previous section. We will quote our best-fit α values and uncertainties (statistical only, leaving consideration of systematic effects to Sect. 6). We will show specifically that the E–B correlation is more constraining than the T–B correlation. This is expected and can be demonstrated directly by computing the variance of Eqs. (5) and (6). For small α, the variance of α based on T–B and E–B information alone is

$$(2\ell+1) f_{\rm sky} (\sigma^{TB}_\ell)^2 \simeq \frac{1}{4}\frac{C^{TT}_\ell C^{BB}_\ell}{(C^{TE}_\ell)^2} \gtrsim \frac{1}{4}\frac{C^{BB}_\ell}{C^{EE}_\ell}, \tag{26}$$

$$(2\ell+1) f_{\rm sky} (\sigma^{EB}_\ell)^2 \simeq \frac{1}{4}\frac{C^{EE}_\ell C^{BB}_\ell}{(C^{EE}_\ell - C^{BB}_\ell)^2} \simeq \frac{1}{4}\frac{C^{BB}_\ell}{C^{EE}_\ell}, \tag{27}$$

respectively. This can be derived from the Fisher information matrix, where the covariance is a simple 1×1 matrix containing the variance of T–B or E–B. Thus, as suggested by the above relations, our results based on E–B are generally more constraining than our T–B results (the presence of noise, however, will modify these relations).

With respect to statistical uncertainty, we will demonstrate that our results are robust to all component-separation methods, and with respect to our two methods. For convenience, we offer a direct comparison of results obtained by our two approaches in Fig. 7.

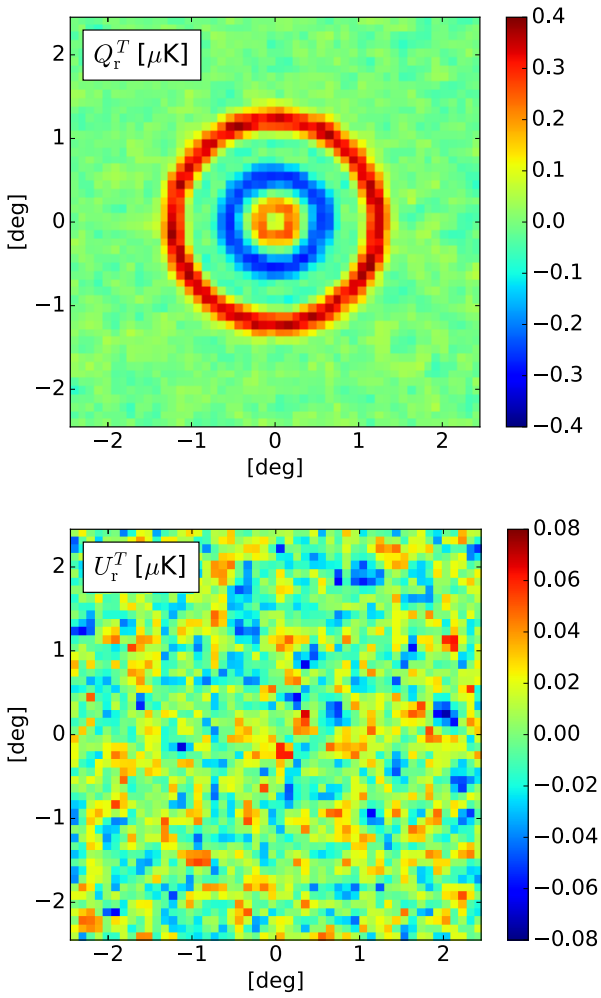

Fig. 1. Stacked images of the transformed Stokes parameters $Q_{\rm r}$ (*top*) and $U_{\rm r}$ (*bottom*) for Commander temperature hot spots. The rotation of the plane of polarization will act to leak the signal from $Q_{\rm r}$ into $U_{\rm r}$. Note that the bottom plot uses a different colour scale to enhance any weak features. Finer resolution stacked images can be seen in Fig. 40 of Planck Collaboration XVI (2016).

5.1. Map-space results

Firstly we note that as a basic check we have verified that Fig. 1 closely reproduces the stacked images shown in Planck Collaboration XVI (2016). We also show the $Q_{\rm r}$ and $U_{\rm r}$ images stacked on E-mode extrema in Fig. 2. The visually striking quadrupole pattern in $U^E_{\rm r}$ appears to be an artefact of the pixelization scheme and is related to the so-called sub-pixel effects described in Planck Collaboration XV (2014) and Planck Collaboration XI (2016). This happens because the pixels of the stacked Q image are imperfectly separated near the centre of the map (the stacked U image does not exhibit this imperfect mixing because the pixel boundaries align perfectly with where the profile changes sign). The pixelization errors are more evident in the $U^E_{\rm r}$ image than the $U^T_{\rm r}$ because the individual Q^E and U^E images are strongly peaked near the centre of the image, and thus when generating the $U_{\rm r}$ stack imperfect subtraction leads to features in the centre of Fig. 2 (bottom). This effect

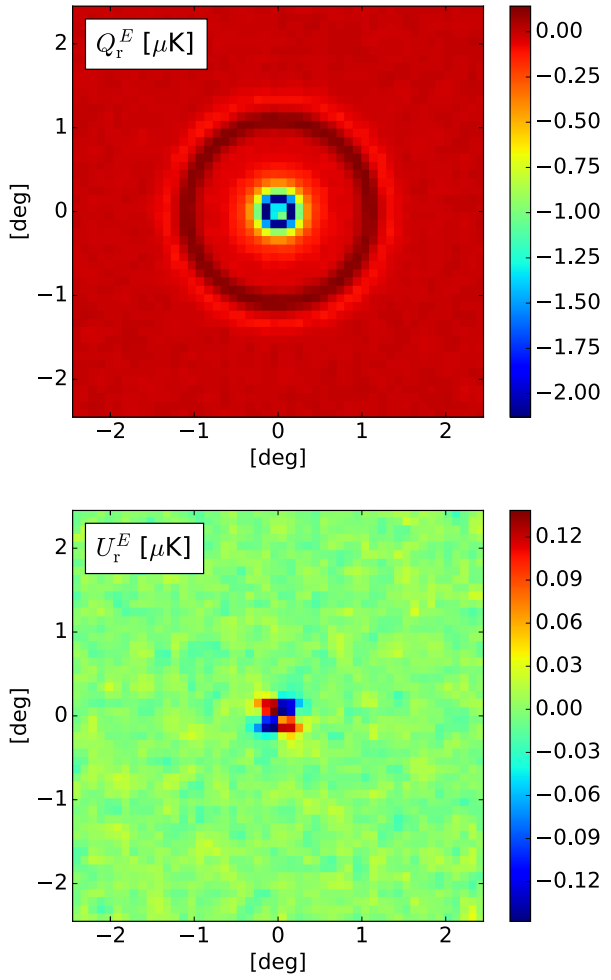

Fig. 2. Stacked images of the transformed Stokes parameters Q_r (*top*) and U_r (*bottom*) for SMICA E-mode hot spots. The rotation of the plane of polarization will act to leak the signal from Q_r into U_r. The quadrupole pattern in the bottom plot is related to subpixel effects (Planck Collaboration XV 2014; Planck Collaboration XI 2016); fortunately, our results are insensitive to this feature, because it disappears in an azimuthal average (see Sect. 5.1).

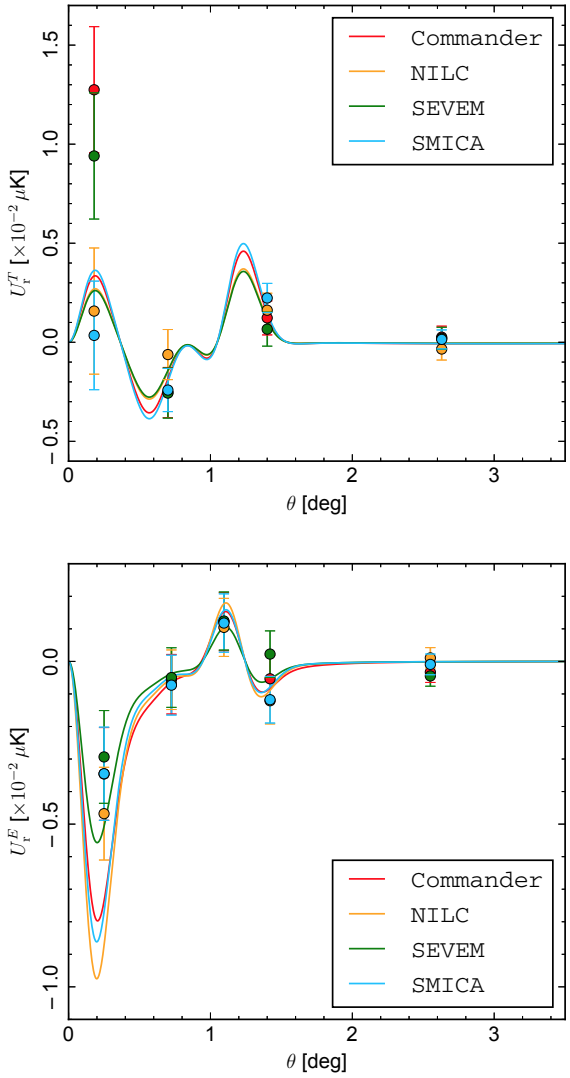

Fig. 3. Profiles of U_r from stacking on temperature (*top*) and E-mode (*bottom*) extrema for the four component-separation methods. The best-fit curves for each component-separation method are also shown, with α values given in the fourth column of Table 1. We have included both hot and cold spots in this figure, i.e., we have co-added the negative of the profile from cold spots to the profile of the hot spots. Error bars correspond to 68% confidence regions.

has a non-diagonal influence on the power spectra and thus has a negligible effect on parameters (Planck Collaboration XV 2014) and this analysis. Alternatively since constraints on α come only from the radial part of the stacked images, the pixelization pattern seen in the centre of Fig. 2, which cancels out in the azimuthal average, will not bias our α results (though it will contribute to the statistical uncertainty).

Figure 3 shows the binned U_r profiles for the four component-separation methods. The apparently non-zero α signal seen in Fig. 3 is not visible in Figs. 1 and 2. This is mainly due to the fact that any signal in the stacked images must be shared out over the 2500 pixels and partially due to the fact that U_r oscillates about zero for $\alpha \neq 0$. The binning here is chosen to pick out ranges with the same sign in the predicted curve for $\alpha \neq 0°$ (with the ΛCDM prediction being identically zero); this choice is for visualization purposes only, since the statistical fit is performed on the original stacked images, i.e., Figs. 1 and 2.

Results are summarized in Tables 1 and 2 for Commander, NILC, SEVEM, and SMICA. Table 1 contains the constraint on α based on the high-pass-filtered Q and U maps and their half-mission half differences (HMHD), which give a useful measure of the noise in the data. We present results based on stacking on temperature and E-mode extrema, both separately and combined. We have estimated that the correlation of the temperature and E-mode stacks are at the sub-percent level by looking at the amount of overlap in the positions of the peaks; thus we can safely neglect correlations in the combined fit. From Table 2 we can see that for most cases $\alpha = 0$ fits the data reasonably well; however, the reduction in χ^2 from a non-zero α is large enough, compared to the expectation of adding a single parameter, to yield a significant detection (with respect to statistical uncertainty only). In other words, while a horizontal line going through 0 μK might seem like an acceptable fit in Fig. 3, a non-zero α is able to pick out the oscillatory features providing a significantly better fit. We report 5–7σ detections for α (with respect to statistical uncertainty only), however, this can be completely explained by a systematic rotation of our polarization-sensitive bolometers (PSBs) which we discuss in Sect. 6. Null-test estimates all give α within 1σ of 0°, with the exception of Commander results stacked on temperature, which

Table 1. Mean values and (1σ) statistical uncertainties for α (in degrees) derived from the stacking analysis for all component-separation methods, coming from hot spots, cold spots, and all extrema.

Method	Hot	Cold	All
	T–B		
Commander	0.36 ± 0.12	0.34 ± 0.11	0.35 ± 0.08
HMHD[a]	-0.13 ± 0.12	-0.20 ± 0.11	-0.16 ± 0.08
NILC[b]	0.23 ± 0.10	0.36 ± 0.10	0.30 ± 0.07
HMHD[a]	-0.08 ± 0.10	0.02 ± 0.10	-0.03 ± 0.07
SEVEM	0.37 ± 0.12	0.18 ± 0.12	0.28 ± 0.08
HMHD[a]	0.07 ± 0.12	0.07 ± 0.12	0.07 ± 0.08
SMICA[b]	0.42 ± 0.10	0.36 ± 0.10	0.39 ± 0.07
HMHD[a]	-0.04 ± 0.10	-0.04 ± 0.10	-0.04 ± 0.07
	E–B		
Commander	0.41 ± 0.11	0.44 ± 0.11	0.43 ± 0.08
HMHD[a]	0.03 ± 0.11	-0.07 ± 0.11	-0.02 ± 0.08
NILC[b]	0.33 ± 0.09	0.38 ± 0.08	0.35 ± 0.06
HMHD[a]	-0.10 ± 0.09	0.01 ± 0.08	-0.05 ± 0.06
SEVEM	0.28 ± 0.12	0.32 ± 0.12	0.30 ± 0.09
HMHD[a]	0.04 ± 0.12	0.04 ± 0.12	0.04 ± 0.09
SMICA[b]	0.25 ± 0.09	0.37 ± 0.09	0.31 ± 0.06
HMHD[a]	-0.11 ± 0.09	0.01 ± 0.09	-0.05 ± 0.06
	Combined		
Commander	0.38 ± 0.08	0.40 ± 0.08	0.39 ± 0.06
HMHD[a]	-0.05 ± 0.08	-0.12 ± 0.08	-0.09 ± 0.06
NILC[b]	0.28 ± 0.06	0.37 ± 0.06	0.33 ± 0.05
HMHD[a]	-0.10 ± 0.06	0.01 ± 0.06	-0.04 ± 0.05
SEVEM	0.32 ± 0.08	0.25 ± 0.08	0.29 ± 0.06
HMHD[a]	0.05 ± 0.09	0.05 ± 0.08	0.05 ± 0.06
SMICA[b]	0.32 ± 0.07	0.37 ± 0.06	0.35 ± 0.05
HMHD[a]	-0.08 ± 0.07	-0.01 ± 0.06	-0.04 ± 0.05

Notes. [(a)] We include the fit from each component-separation method's half-mission half-difference (HMHD) Q and U maps, as an indication of the expectation for noise. [(b)] NILC and SMICA have smaller uncertainties compared with Commander and SEVEM, which follows from the naive expectation of the rms in the polarization maps (see Table 1 of Planck Collaboration IX 2016).

are slightly above 1σ (see the second and eighteenth rows of Table 1). We have also checked that there is very weak dependence on our results coming from the different choices for the thresholds used to define the peaks.

A stacking analysis similar to ours has been attempted in Contaldi (2015) also using *Planck* data. Our results based on *E–B* data are consistent with those of Contaldi (2015), but with smaller statistical uncertainties; however, we disagree with Contaldi (2015) regarding the constraints coming from *T–B* data, which are claimed to be too noisy to be used. We show here that both *T–B* and *E–B* data can be successfully exploited to constrain the birefringence angle.

5.2. Harmonic-space results

Following the recommendation given by the *Planck* collaboration (Planck Collaboration IX 2016), we present results below based only on cross-correlations. Therefore, as described in Sect. 3, we present results for the D^{TB}-estimator using the full-mission data from Commander, NILC, SEVEM, and SMICA, and with half-mission data for SMICA. For the same reasons we present results with the D^{EB}-estimator using the half-mission data from SMICA only. Additionally we present a joint analysis with the half-mission data from SMICA. Of course the *D*-estimators are built through the CMB angular power spectra. As an example, we display in Fig. 4 the *TB* and *EB* CMB angular power spectra obtained with the SMICA method using half-mission data. We also show the FFP8.1 simulations for the same component-separation method.

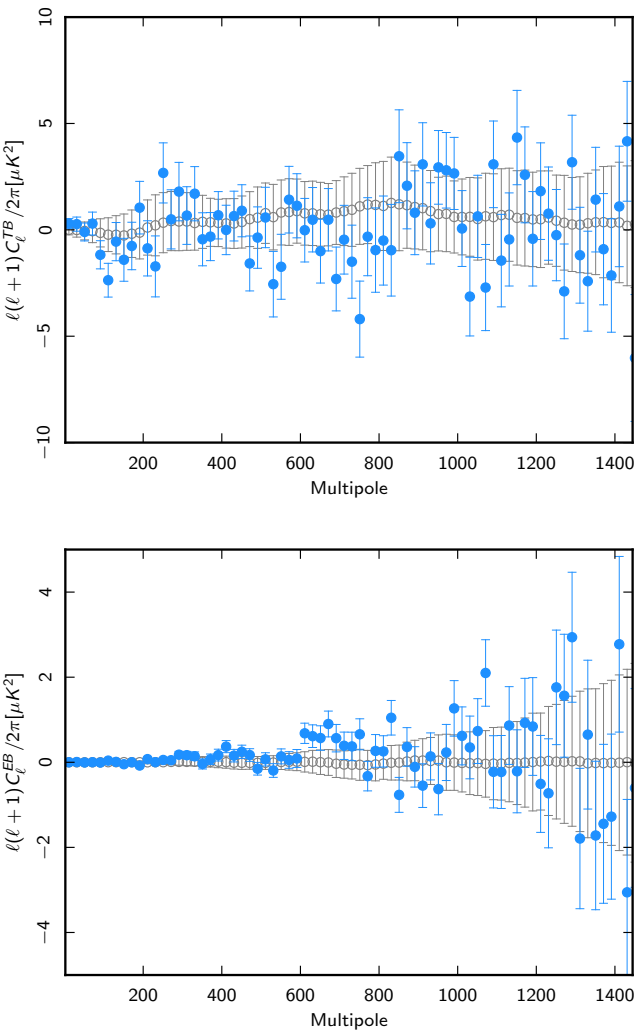

Fig. 4. Angular power spectrum estimates for *TB* (*top*) and *EB* (*bottom*), with SMICA data in blue and the corresponding simulations in black. Only statistical uncertainties are shown here.

5.2.1. *T–B*

The estimates obtained are displayed in Fig. 5 as a function of the maximum multipole considered ($\ell_{\rm max}$). We note that all the estimates are stable among the component-separation methods and against the choice of $\ell_{\rm max}$. Moreover, the SMICA results provide a further test of stability with respect to computing the CMB angular power spectra from full-mission or half-mission data and simulations. The estimates of the birefringence angle for $\ell_{\rm max} \simeq 1500$ are also reported in Table 3 (see first five rows for D_ℓ^{TB}).

Table 2. χ^2 values for the model with $\alpha = 0$, derived from the stacking analysis for all component-separation methods.

Method	Hot			Cold		
	χ^{2a}	$\Delta\chi^2$	PTE	χ^{2a}	$\Delta\chi^2$	PTE
			T–B			
Commander	2453.7	−9.2	1.2×10^{-3}	2769.8	−9.3	1.1×10^{-3}
NILC	2525.8	−5.2	1.1×10^{-2}	2641.3	−13.3	1.3×10^{-4}
SEVEM	2552.6	−9.7	9.4×10^{-4}	2718.9	−2.3	6.4×10^{-2}
SMICA	2567.7	−17.2	1.7×10^{-5}	2610.1	−13.0	1.5×10^{-4}
			E–B			
Commander	2548.8	−12.1	2.5×10^{-4}	2542.7	−15.9	3.3×10^{-5}
NILC	2554.4	−13.3	1.3×10^{-4}	2555.9	−19.3	5.7×10^{-6}
SEVEM	2551.5	−4.6	1.6×10^{-2}	2552.0	−6.7	4.8×10^{-3}
SMICA	2556.8	−7.9	2.5×10^{-3}	2559.1	−17.2	1.7×10^{-5}

Notes. The $\Delta\chi^2$ is the reduction of χ^2 given the values of α in the corresponding entry in Table 1. For convenience we have also included the probability to exceed (PTE) for each value of α. [(a)] The number of degrees of freedom is 2500 coming from a $5^\circ \times 5^\circ$ patch with $0.^\circ1$ pixel size.

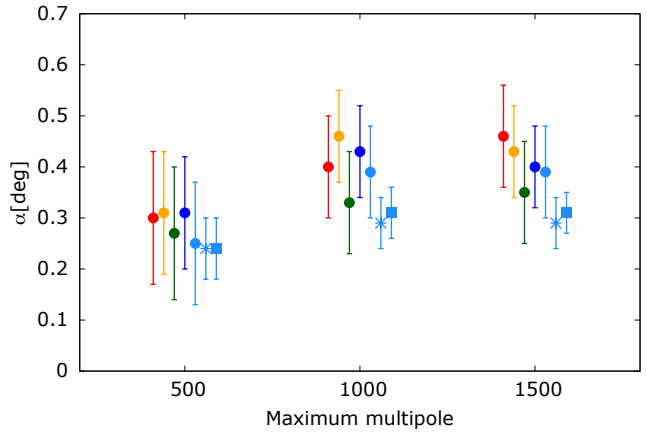

Fig. 5. Birefringence angle estimates (in degrees) versus the maximum multipole considered. Only (1σ) statistical uncertainties are shown here; with systematic errors discussed later. Commander is shown in red, NILC in orange, SEVEM in green, SMICA (full-mission data) in blue, and SMICA (half-mission data) in cyan. Dot symbols refer to the estimates obtained with the D_ℓ^{TB} estimator. Star symbols refer to estimates coming from D_ℓ^{EB} and squares are obtained through the combination of D_ℓ^{TB} and D_ℓ^{EB}.

In Fig. 6 we show the dependence of α on angular scale[9]. This is built by considering Eq. (25) applied to D_ℓ^{TB}. Comparing the different component-separation methods and the different ways of estimating the spectra, we find good stability of the α estimates for each angular scale. The statistical uncertainties follow the behavior described in Gruppuso et al. (2016).

5.2.2. *E–B*

Considering Eq. (24) for the estimator D_ℓ^{EB}, defined in Eq. (20), we have extracted the birefringence angle α for the half-mission SMICA data. The estimate obtained for α is given in Table 3 (see sixth row) and is compatible with constraints from the other component-separation methods, as is also clear from Fig. 5. Figure 6 shows the spectrum of α obtained in this case. We note that the statistical uncertainty coming from D_ℓ^{EB} is much smaller than that obtained from D_ℓ^{TB}. This is expected since Eqs. (26) and (27) suggests that the E–B correlation is able to constrain α better than the T–B correlation.

Table 3. Minimum χ^2 values and statistical uncertainties (1σ) for α, derived from the D-estimators with $\ell_{\rm max} \simeq 1500$.

Method	α [deg]	bias[a] [deg]	$\chi^2(\alpha = 0)$	$\Delta\chi^{2d}$
		T–B		
Commander	0.44 ± 0.10	0.01	87.1	−20.9
NILC[b]	0.43 ± 0.09	−0.01	104.3	−22.5
SEVEM	0.31 ± 0.10	0.02	80.0	−10.3
SMICA[b]	0.40 ± 0.08	0.00	92.7	−23.9
SMICA×[b,c]	0.39 ± 0.09	−0.01	92.8	−18.8
		E–B		
SMICA×[b,c]	0.29 ± 0.05	0.00	135.9	−39.9
		Combined		
SMICA×[b,c]	0.31 ± 0.05	0.00	228.7	−57.9

Notes. The χ^2 values for $\alpha = 0$ and the change $\Delta\chi^2$ for the corresponding value of the birefringence angle are provided in the fourth and fifth columns respectively. [(a)] The bias refers to the average value of α determined using the corresponding FFP8.1 simulations. [(b)] NILC and SMICA have smaller uncertainties compared with Commander and SEVEM, which follows from the naive expectation of the rms in the polarization maps (see Table 1 of Planck Collaboration IX 2016). [(c)] The × symbol denotes the cross-correlation of half-mission 1 with half-mission 2 data. [(d)] The corresponding probability to exceed is always below 1/1000 except for SEVEM which turns out to be 2/1000.

5.2.3. *T–B* and *E–B* combined

The CMB power spectra from the SMICA cross-correlations allow us to build a joint estimate minimizing the total χ^2, defined as $\chi^2(\alpha) = \chi^2_{TB}(\alpha) + \chi^2_{EB}(\alpha)$. We have explicitly checked with

[9] This should not be confused with a spectrum of the birefringence anisotropies. As stated in Sect. 2 in this paper we are only concerned with a uniform rotation.

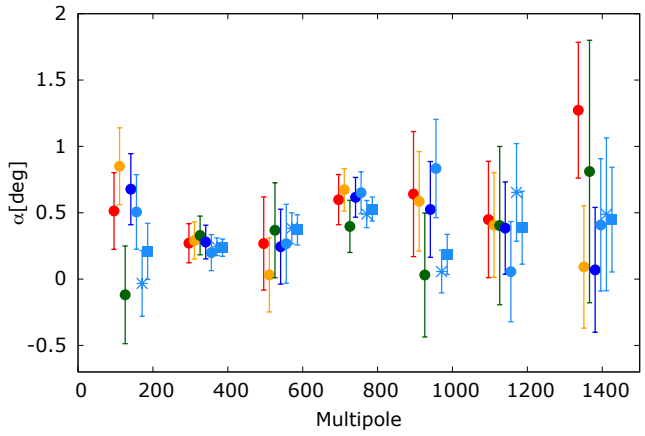

Fig. 6. Spectrum of α in degrees versus multipole. As in Fig. 5 only (1σ) statistical uncertainties are shown. The colour coding is the same as in Fig. 5. See also footnote 9.

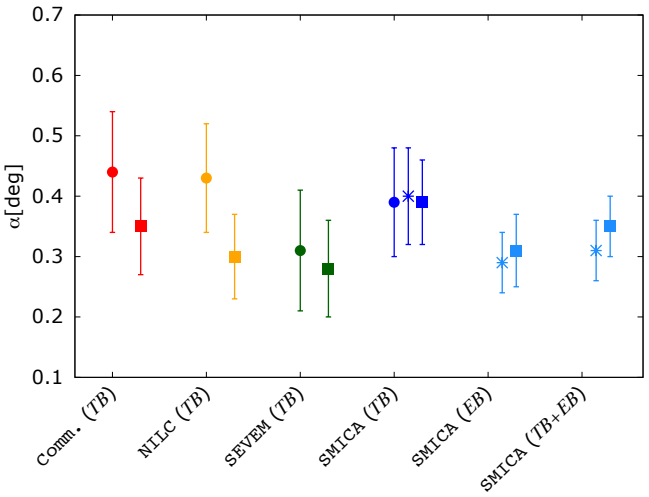

Fig. 7. Comparison between harmonic and pixel-based analysis. Dot (star) symbols show the estimates coming from D-estimators built with CMB spectra obtained from full-mission (half-mission) data. Square symbols represent the estimates coming from the stacking analysis.

FFP8.1 simulations that there is no significant cross-correlation between D_{TB} and D_{EB}[10] and this in turn means that it is possible to minimize the simple sum of χ^2. Not surprisingly, it turns out that such a combination is dominated by the E–B correlation information. The obtained constraint is reported again in Table 3 (see last row) and in Fig. 5. As before, in Fig. 6 we provide the spectrum of α obtained from minimizing χ^2 in intervals of ℓ. The overall consistency of each estimate is always very good.

6. Systematic effects

The main systematic effect that is completely degenerate with the signal from isotropic cosmological birefringence is uncertainty in the orientation of the PSBs used for mapmaking (Pagano et al. 2009). The nature of this error is characterized in the PCCS2 paper (Planck Collaboration XXVI 2016), as well as HFI (Planck Collaboration VII 2016; Planck Collaboration VIII 2016) and LFI (Leahy et al. 2010; Planck Collaboration III 2014; Planck Collaboration IV 2014) systematics papers, and also described in Planck Collaboration XLVI (2016). The present upper limit in any global rotation of the HFI detectors is estimated to be better than 0.°3; however, the *relative* upper limit between separate PSBs is 0.°9 (Rosset et al. 2010). After converting the above numbers into standard deviations (assuming they are approximately uniform distributions, and noting that the relative uncertainty can be averaged over the eight PSBs used by *Planck*) we conservatively quote the total (global and relative) 1σ uncertainty as 0.°28. This final error is not exactly Gaussian, although it is close (68% and 95% CLs are 0.°28 and 0.°55, respectively). Given that we detect a rotation of around 0.°3, we are, therefore, unable to disentangle the signal found in the data from the possible presence of this systematic effect. It remains to be seen whether or not this can be improved in a future *Planck* release.

It might be expected that `Commander` would perform best in polarization in terms of noise and handling of systematics (based on the angular scales probed here, see Planck Collaboration IX 2016, for details). However, given that `Commander` uses a slightly different set of data than the other component-separation methods and given that they all use different algorithms, we cannot make any definitive claims as to which gives the most accurate constraint. We are also unable to account for the apparent discrepancy at the roughly 2σ level (given the large number of comparisons performed here, this could simply be a statistical fluke) that the `Commander` noise estimate yields for α when stacking on temperature (see Table 1). That being said, it is reassuring that all component-separation methods agree at the $\simeq 1\sigma$ level in their constraints on α.

In the following subsections we mention some other possible systematic effects that might be present, but that we believe contribute negligibly to the polarization rotation signal.

6.1. Noise properties of polarization

The recommendation from the *Planck* collaboration is that any analysis performed on polarization data should not be very sensitive to mis-characterization of the noise. To this end cross-spectra, cross-correlation, and stacking analyses are examples of such approaches. Our harmonic space and map space temperature tests fulfil this criterion explicitly. It is less obvious that stacking on E-mode extrema should only weakly depend on the noise properties; however, we find this to be the case. This is because the statistics of the E-mode map are encoded in the bias parameters $(\bar{b}_\nu, \bar{b}_\zeta)$, which depend on the *total* power in the map (see Appendix A for details). Therefore the bias parameters will be accurate to the level that the statistics of the polarization data can be determined by its two-point function. Nevertheless we will now describe to what extent a miscalculation of the bias parameters will affect our results.

We use the `MASTER` method (to correct for masking, Hivon et al. 2002) to estimate the total power spectrum of the E-mode map in order to calculate the bias parameters $(\bar{b}_\nu, \bar{b}_\zeta)$. The noise term in Eq. (11) is then given by subtracting the theoretical power spectrum (C_ℓ^{EE}) from the total power spectrum. The main effect of noise, however, comes from the determination of the bias terms only since most of the discriminatory power on α comes from the U_r stacks (Eqs. (12) and (16) do not explicitly depend on the noise term).

[10] The impact of taking such a cross-correlation into account is at most at the level of half of the statistical standard deviation.

The largest difference in our noise estimation when comparing between different component-separation methods comes from SEVEM and SMICA. For these maps $\bar{b}_\mu$ differs by approximately 20%, and $\bar{b}_\zeta$ by 40%. Using the SEVEM bias parameter values on the SMICA data (for example) leads to a roughly 1σ shift in the posterior of α (from E-modes). Such a discrepancy estimate is overly conservative, however, because each component-separation technique will generally produce maps with different noise levels. If instead we scale our noise estimate by as much as 10% (for any of the individual component-separation methods) we find that α shifts by less than 0.25σ. We therefore conclude that for our analysis, mis-characterization of the noise in polarization has little to no effect.

6.2. Beam effects

Because of the differential nature of polarization measurements, any beam mismatch or uncertainties can induce temperature-to-polarization leakage (Hu et al. 2003; Leahy et al. 2010). Here we are interested in beam uncertainties that can potentially lead to T–B and E–B correlations that might mimic a non-zero α signal. Due to circular symmetry, effects from differential beam sizes or differential relative gains will not tend to produce T–B or E–B correlations, whereas effects from differential pointing and differential ellipticity will. Differences in the noise level will also in general cause temperature-to-polarization leakage.

We check for these effects following the approach described in Planck Collaboration XI (2016) and Planck Collaboration XIII (2016). It should be noted that temperature-to-polarization leakage estimates due to bandpass mismatches between detectors have been removed from the component-separated maps (see Planck Collaboration IV 2016; Planck Collaboration VI 2016; Planck Collaboration VIII 2016; Planck Collaboration IX 2016, for details); we perform a crude scan of the parameter space in the following temperature-to-polarization leakage model (see also Appendix A.6 of Planck Collaboration XLVI 2016):

$$C_\ell^{TE} \rightarrow C_\ell^{TE} + \epsilon C_\ell^{TT}; \tag{28}$$

$$C_\ell^{TB} \rightarrow \beta C_\ell^{TT}; \tag{29}$$

$$C_\ell^{EE} \rightarrow C_\ell^{EE} + \epsilon^2 C_\ell^{TT} + 2\epsilon C_\ell^{TE}; \tag{30}$$

$$C_\ell^{EB} \rightarrow \epsilon\beta_\ell C_\ell^{TT} + \beta C_\ell^{TE}. \tag{31}$$

The ϵ and β terms are expected to be dominated by $m = 2$ and $m = 4$ modes (assuming the mismatch comes from differential ellipticity) and can be written as

$$\epsilon = \epsilon_2 \ell^2 + \epsilon_4 \ell^4, \tag{32}$$

$$\beta = \beta_2 \ell^2 + \beta_4 \ell^4. \tag{33}$$

Varying (ϵ_2, β_2), and (ϵ_4, β_4) in the range given by $\sigma_2 = 1.25 \times 10^{-8}$, and $\sigma_4 = 2.7 \times 10^{-15}$ (Planck Collaboration XI 2016), we find that α is stable to $<0.1\sigma$ (this is the case for both temperature and E-mode stacks).

We must stress, however, that the above temperature-to-polarization leakage model is not completely satisfactory (see Sect. 3.4.3 and Appendix C.3.5 in Planck Collaboration XI 2016, for full details). Nevertheless it is adequate for our purposes since we only wish to demonstrate that our results remain stable to most forms of beam mismatch.

7. Conclusions

We have estimated the rotation, α, of the plane of polarization of CMB photons by using *Planck* 2015 data. Employing harmonic-space cross-correlations and a map-space stacking approach we find values of 0.°31 and 0.°35, respectively, for the angle α (using SMICA data). Both methods yield the same statistical uncertainty, i.e., 0.°05 (68% CL), and are subject to the same systematic error of 0.°28 (68% CL) due to the uncertainty in the global and relative orientations of the PSBs. Our results are compatible with no rotation, i.e., no parity violation, within the total error budget. We have demonstrated that our findings are robust against two independent analysis approaches, different component-separation methods, harmonic scales, choices in peak thresholds, and temperature-to-polarization leakage, at better than the 1σ statistical level. We have also carefully chosen our analyses to be insensitive to detailed knowledge of the noise properties of the polarization data. It should be noted that the statistical and systematic error bars represent our best knowledge of the *Planck* data at the time of publication[11]. Several additional effects have the potential to enlarge the error estimates. Among the possible source of extra systematics are residuals from the processing, which are only partially captured by the FFP8.1 simulations since these simulations do not yet include all the details of the instruments. In Planck Collaboration XI (2016) we analysed a few end-to-end simulations from HFI, which include more systematic effects than those contained in FFP8.1, and found no evidence for significant influence on the results of the TT likelihood. Planck Collaboration XLVI (2016) shows that the FFP8 simulations fail to capture most of the very low ell ($\ell < 30$) polarization systematics. Our measurement here, based on multipoles larger than $\ell = 50$ should be immune to these sorts of issues, but there are not enough end-to-end simulations available at this time to definitively prove this. Similarly, we relied on the efficiency of component-separated maps to treat the Galactic residuals. This assumes that the FFP8 Galactic model correctly describes TB and EB induced correlation. Comparing the estimates obtained from different component-separation methods, we expect that the latter uncertainty is at most of the order of 1σ statistical error.

In Fig. 8 we show a comparison of our estimate with the birefringence angle estimates provided by analysis on other CMB data in which, where possible, the total error budget is decomposed in these two parts, i.e., statistical (left point of a pair) and systematic (right). The total error budget of our estimate is dominated by the systematic uncertainty, which is a factor of 6 larger than the statistical one. It is clear, therefore, that future CMB polarization experiments (or a future *Planck* release) will require a much better understanding of their polarimeter orientations since this is the current limiting factor of this investigation. With a coordination of careful ground-based measurements and improved in-flight calibration on polarized sources (see Kaufman et al. 2014, for an example of a possible effort) we may be able to further probe possible parity violations in the Universe.

[11] We do not recommend the use of any TB, and EB information (either in form of spectra, stacking or any other estimator that depends on the cross-correlation between T and B modes or E and B modes) without including in the analysis the uncertainty coming from the instrumental polarization angle (and other systematic effects that might dominate the error budget).

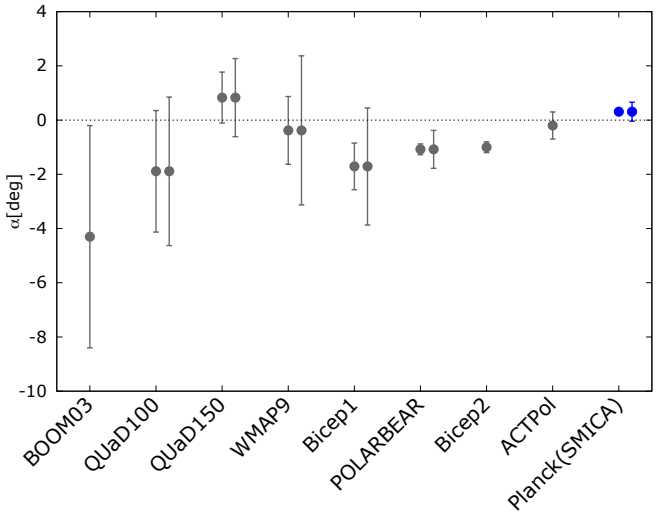

Fig. 8. Constraints on α coming from published analyses of several sets of CMB experimental data sets (shown in grey) as reviewed in Kaufman et al. (2016) compared with what is found in the present paper (in blue). For each experiment the left error bars are for statistical uncertainties at 68% CL, while right error bars (when displayed) are obtained by summing linearly the statistical and systematic uncertainties. The error bar of BOOM03 already contains a contribution from systematic effects.

Acknowledgements. The Planck Collaboration acknowledges the support of: ESA; CNES, and CNRS/INSU-IN2P3-INP (France); ASI, CNR, and INAF (Italy); NASA and DoE (USA); STFC and UKSA (UK); CSIC, MINECO, JA, and RES (Spain); Tekes, AoF, and CSC (Finland); DLR and MPG (Germany); CSA (Canada); DTU Space (Denmark); SER/SSO (Switzerland); RCN (Norway); SFI (Ireland); FCT/MCTES (Portugal); ERC and PRACE (EU). A description of the Planck Collaboration and a list of its members, indicating which technical or scientific activities they have been involved in, can be found at http://www.cosmos.esa.int/web/planck/planck-collaboration. Some of the results of this paper have been derived using the HEALPix package (Górski et al. 2005).

References

Ade, P. A. R., Akiba, Y., Anthony, A. E., et al. 2014a, ApJ, 794, 171
Ade, P. A. R., Aikin, R. W., Amiri, M., et al. 2014b, ApJ, 792, 62
Ade, P. A. R., Arnold, K., Atlas, M., et al. 2015, Phys. Rev. D, 92, 123509
Bielewicz, P., Banday, A. J., & Górski, K. M. 2012, MNRAS, 421, 1064
Bond, J. R., & Efstathiou, G. 1987, MNRAS, 226, 655
Brown, M. L., Ade, P., Bock, J., et al. 2009, ApJ, 705, 978
Carroll, S. M. 1998, Phys. Rev. Lett., 81, 3067
Carroll, S. M., Field, G. B., & Jackiw, R. 1990, Phys. Rev. D, 41, 1231
Cimatti, A., di Serego-Alighieri, S., Fosbury, R. A. E., Salvati, M., & Taylor, D. 1993, MNRAS, 264, 421
Cimatti, A., de Serego Alighieri, S., Field, G. B., & Fosbury, R. A. E. 1994, ApJ, 422, 562
Contaldi, C. R. 2015, ArXiv e-prints [arXiv:1510.02629]
Desjacques, V. 2008, Phys. Rev. D, 78, 103503
di Serego Alighieri, S., Finelli, F., & Galaverni, M. 2010, ApJ, 715, 33
di Serego Alighieri, S., Ni, W.-T., & Pan, W.-P. 2014, ApJ, 792, 35
Feng, B., Li, H., Li, M., & Zhang, X. 2005, Phys. Lett. B, 620, 27
Feng, B., Li, M., Xia, J.-Q., Chen, X., & Zhang, X. 2006, Phys. Rev. Lett., 96, 221302
Finelli, F., & Galaverni, M. 2009, Phys. Rev. D, 79, 063002
Gluscevic, V., Hanson, D., Kamionkowski, M., & Hirata, C. M. 2012, Phys. Rev. D, 86, 103529
Górski, K. M., Hivon, E., Banday, A. J., et al. 2005, ApJ, 622, 759
Gruppuso, A., Natoli, P., Mandolesi, N., et al. 2012, J. Cosmol. Astropart. Phys., 1202, 023
Gruppuso, A., Gerbino, M., Natoli, P., et al. 2015, J. Cosmol. Astropart. Phys., 6, 001
Gruppuso, A., Maggio, G., Molinari, D., & Natoli, P. 2016, J. Cosmol. Astropart. Phys., 1605, 020
Gubitosi, G., Martinelli, M., & Pagano, L. 2014, J. Cosmol. Astropart. Phys., 12, 20
Hinshaw, G., et al. 2013, ApJS, 208, 19
Hivon, E., Górski, K. M., Netterfield, C. B., et al. 2002, ApJ, 567, 2
Hu, W., Hedman, M. M., & Zaldarriaga, M. 2003, Phys. Rev. D, 67, 043004
Kamionkowski, M. 2010, Phys. Rev. D, 82, 047302
Kamionkowski, M., Kosowsky, A., & Stebbins, A. 1997, Phys. Rev. D, 55, 7368
Kaufman, J. P., Miller, N. J., Shimon, M., et al. 2014, Phys. Rev. D, 89, 062006
Kaufman, J. P., Keating, B. G., & Johnson, B. R. 2016, MNRAS, 455, 1981
Keating, B., Shimon, M., & Yadav, A. 2012, ApJ, 762, L23
Kim, J. 2011, A&A, 531, A32
Kogut, A., Spergel, D. N., Barnes, C., et al. 2003, ApJS, 148, 161
Komatsu, E., Smith, K. M., Dunkley, J., et al. 2011, ApJS, 192, 18
Leahy, J. P. 1997, ArXiv e-prints [arXiv:astro-ph/9704285]
Leahy, J. P., Bersanelli, M., D'Arcangelo, O., et al. 2010, A&A, 520, A8
Li, M., & Zhang, X. 2008, Phys. Rev. D, 78, 103516
Li, M., Cai, Y.-F., Wang, X., & Zhang, X. 2009, Phys. Lett. B, 680, 118
Liu, G.-C., Lee, S., & Ng, K.-W. 2006, Phys. Rev. Lett., 97, 161303
Lue, A., Wang, L., & Kamionkowski, M. 1999, Phys. Rev. Lett., 83, 1506
Mei, H.-H., Ni, W.-T., Pan, W.-P., Xu, L., & di Serego Alighieri, S. 2015, ApJ, 805, 107
Molinari, D., Gruppuso, A., & Natoli, P. 2016, Physics of the Dark Universe, 14, 65
Naess, S., Hasselfield, M., McMahon, J., et al. 2014, J. Cosmol. Astropart. Phys., 10, 7
Pagano, L., de Bernardis, P., de Troia, G., et al. 2009, Phys. Rev. D, 80, 043522
Planck Collaboration III. 2014, A&A, 571, A3
Planck Collaboration IV. 2014, A&A, 571, A4
Planck Collaboration XV. 2014, A&A, 571, A15
Planck Collaboration I. 2016, A&A, 594, A1
Planck Collaboration IV. 2016, A&A, 594, A4
Planck Collaboration VI. 2016, A&A, 594, A6
Planck Collaboration VII. 2016, A&A, 594, A7
Planck Collaboration VIII. 2016, A&A, 594, A8
Planck Collaboration IX. 2016, A&A, 594, A9
Planck Collaboration X. 2016, A&A, 594, A10
Planck Collaboration XI. 2016, A&A, 594, A11
Planck Collaboration XII. 2016, A&A, 594, A12
Planck Collaboration XIII. 2016, A&A, 594, A13
Planck Collaboration XVI. 2016, A&A, 594, A16
Planck Collaboration XXVI. 2016, A&A, 594, A26
Planck Collaboration Int. XLVI. 2016, A&A, 596, A107
Polenta, G., Marinucci, D., Balbi, A., et al. 2005, J. Cosmol. Astropart. Phys., 11, 1
Rosset, C., Tristram, M., Ponthieu, N., et al. 2010, A&A, 520, A13
Wardle, J. F. C., Perley, R. A., & Cohen, M. H. 1997, Phys. Rev. Lett., 79, 1801
Wu, E. Y. S., Ade, P., Bock, J., et al. 2009, Phys. Rev. Lett., 102, 161302
Zaldarriaga, M., & Seljak, U. 1997, Phys. Rev. D, 55, 1830
Zhao, G.-B., Wang, Y., Xia, J.-Q., Li, M., & Zhang, X. 2015, J. Cosmol. Astropart. Phys., 1507, 032

[1] APC, AstroParticule et Cosmologie, Université Paris Diderot, CNRS/IN2P3, CEA/lrfu, Observatoire de Paris, Sorbonne Paris Cité, 10 rue Alice Domon et Léonie Duquet, 75205 Paris Cedex 13, France
[2] African Institute for Mathematical Sciences, 6-8 Melrose Road, Muizenberg 7945, Cape Town, South Africa
[3] Agenzia Spaziale Italiana Science Data Center, via del Politecnico snc, 00133 Roma, Italy
[4] Astrophysics Group, Cavendish Laboratory, University of Cambridge, J J Thomson Avenue, Cambridge CB3 0HE, UK
[5] Astrophysics & Cosmology Research Unit, School of Mathematics, Statistics & Computer Science, University of KwaZulu-Natal, Westville Campus, Private Bag X54001, Durban 4000, South Africa
[6] CITA, University of Toronto, 60 St. George St., Toronto, ON M5S 3H8, Canada
[7] CNRS, IRAP, 9 Av. colonel Roche, BP 44346, 31028 Toulouse Cedex 4, France
[8] California Institute of Technology, Pasadena, CA 91125, USA
[9] Computational Cosmology Center, Lawrence Berkeley National Laboratory, Berkeley, CA 94720, USA
[10] Département de Physique Théorique, Université de Genève, 24 quai E. Ansermet, 1211 Genève 4, Switzerland
[11] Departamento de Astrofísica, Universidad de La Laguna (ULL), 38206 La Laguna, Tenerife, Spain
[12] Departamento de Física, Universidad de Oviedo, Avda. Calvo Sotelo s/n, 33007 Oviedo, Spain

[13] Department of Astrophysics/IMAPP, Radboud University Nijmegen, PO Box 9010, 6500 GL Nijmegen, The Netherlands
[14] Department of Physics & Astronomy, University of British Columbia, 6224 Agricultural Road, Vancouver, British Columbia, Canada
[15] Department of Physics and Astronomy, Dana and David Dornsife College of Letter, Arts and Sciences, University of Southern California, Los Angeles, CA 90089, USA
[16] Department of Physics and Astronomy, University College London, London WC1E 6BT, UK
[17] Department of Physics and Astronomy, University of Sussex, Brighton BN1 9QH, UK
[18] Department of Physics, Gustaf Hällströmin katu 2a, University of Helsinki, Helsinki, Finland
[19] Department of Physics, Princeton University, Princeton, NJ 08544, USA
[20] Department of Physics, University of California, Santa Barbara, CA 93106, USA
[21] Department of Physics, University of Illinois at Urbana-Champaign, 1110 West Green Street, Urbana, Illinois, USA
[22] Dipartimento di Fisica e Astronomia G. Galilei, Università degli Studi di Padova, via Marzolo 8, 35131 Padova, Italy
[23] Dipartimento di Fisica e Astronomia, Alma Mater Studiorum, Università degli Studi di Bologna, Viale Berti Pichat 6/2, 40127 Bologna, Italy
[24] Dipartimento di Fisica e Scienze della Terra, Università di Ferrara, via Saragat 1, 44122 Ferrara, Italy
[25] Dipartimento di Fisica, Università La Sapienza, P.le A. Moro 2, 00185 Roma, Italy
[26] Dipartimento di Fisica, Università degli Studi di Milano, via Celoria 16, 20133 Milano, Italy
[27] Dipartimento di Fisica, Università degli Studi di Trieste, via A. Valerio 2, 34127 Trieste, Italy
[28] Dipartimento di Fisica, Università di Roma Tor Vergata, via della Ricerca Scientifica 1, 00133 Roma, Italy
[29] Dipartimento di Matematica, Università di Roma Tor Vergata, via della Ricerca Scientifica 1, 00133 Roma, Italy
[30] European Space Agency, ESAC, Planck Science Office, Camino bajo del Castillo, s/n, Urbanización Villafranca del Castillo, 28692 Villanueva de la Cañada, Madrid, Spain
[31] European Space Agency, ESTEC, Keplerlaan 1, 2201 AZ Noordwijk, The Netherlands
[32] Gran Sasso Science Institute, INFN, viale F. Crispi 7, 67100 L'Aquila, Italy
[33] HGSFP and University of Heidelberg, Theoretical Physics Department, Philosophenweg 16, 69120 Heidelberg, Germany
[34] Helsinki Institute of Physics, Gustaf Hällströmin katu 2, University of Helsinki, 00014 Helsinki, Finland
[35] INAF–Osservatorio Astronomico di Padova, Vicolo dell'Osservatorio 5, 35122 Padova, Italy
[36] INAF–Osservatorio Astronomico di Roma, via di Frascati 33, 00040 Monte Porzio Catone, Italy
[37] INAF–Osservatorio Astronomico di Trieste, via G. B. Tiepolo 11, 40127 Trieste, Italy
[38] INAF/IASF Bologna, via Gobetti 101, 40129 Bologna, Italy
[39] INAF/IASF Milano, via E. Bassini 15, 20133 Milano, Italy
[40] INFN – CNAF, viale Berti Pichat 6/2, 40127 Bologna, Italy
[41] INFN, Sezione di Bologna, viale Berti Pichat 6/2, 40127 Bologna, Italy
[42] INFN, Sezione di Ferrara, via Saragat 1, 44122 Ferrara, Italy
[43] INFN, Sezione di Roma 1, Università di Roma Sapienza, P.le Aldo Moro 2, 00185 Roma, Italy
[44] INFN, Sezione di Roma 2, Università di Roma Tor Vergata, via della Ricerca Scientifica 1, 00185 Roma, Italy
[45] IPAG: Institut de Planétologie et d'Astrophysique de Grenoble, Université Grenoble Alpes, IPAG; CNRS, IPAG, 38000 Grenoble, France
[46] Imperial College London, Astrophysics group, Blackett Laboratory, Prince Consort Road, London, SW7 2AZ, UK
[47] Institut d'Astrophysique Spatiale, CNRS, Univ. Paris-Sud, Université Paris-Saclay, Bât. 121, 91405 Orsay Cedex, France
[48] Institut d'Astrophysique de Paris, CNRS (UMR 7095), 98bis boulevard Arago, 75014 Paris, France
[49] Institute of Astronomy, University of Cambridge, Madingley Road, Cambridge CB3 0HA, UK
[50] Institute of Theoretical Astrophysics, University of Oslo, Blindern, 0371 Oslo, Norway
[51] Instituto de Astrofísica de Canarias, C/Vía Láctea s/n, La Laguna, 38205 Tenerife, Spain
[52] Instituto de Física de Cantabria (CSIC-Universidad de Cantabria), Avda. de los Castros s/n, 39005 Santander, Spain
[53] Istituto Nazionale di Fisica Nucleare, Sezione di Padova, via Marzolo 8, 35131 Padova, Italy
[54] Jet Propulsion Laboratory, California Institute of Technology, 4800 Oak Grove Drive, Pasadena, CA 31109, USA
[55] Jodrell Bank Centre for Astrophysics, Alan Turing Building, School of Physics and Astronomy, The University of Manchester, Oxford Road, Manchester, M13 9PL, UK
[56] Kavli Institute for Cosmological Physics, University of Chicago, Chicago, IL 60637, USA
[57] Kavli Institute for Cosmology Cambridge, Madingley Road, Cambridge, CB3 0HA, UK
[58] LAL, Université Paris-Sud, CNRS/IN2P3, 91898 Orsay, France
[59] LERMA, CNRS, Observatoire de Paris, 61 avenue de l'Observatoire, 75014 Paris, France
[60] Laboratoire Traitement et Communication de l'Information, CNRS (UMR 5141) and Télécom ParisTech, 46 rue Barrault, 75634 Paris Cedex 13, France
[61] Laboratoire de Physique Subatomique et Cosmologie, Université Grenoble-Alpes, CNRS/IN2P3, 53 rue des Martyrs, 38026 Grenoble Cedex, France
[62] Laboratoire de Physique Théorique, Université Paris-Sud 11 & CNRS, Bâtiment 210, 91405 Orsay, France
[63] Max-Planck-Institut für Astrophysik, Karl-Schwarzschild-Str. 1, 85741 Garching, Germany
[64] Mullard Space Science Laboratory, University College London, Surrey RH5 6NT, UK
[65] Nicolaus Copernicus Astronomical Center, Bartycka 18, 00-716 Warsaw, Poland
[66] Nordita (Nordic Institute for Theoretical Physics), Roslagstullsbacken 23, 106 91 Stockholm, Sweden
[67] SISSA, Astrophysics Sector, via Bonomea 265, 34136 Trieste, Italy
[68] School of Chemistry and Physics, University of KwaZulu-Natal, Westville Campus, Private Bag X54001, Durban 4000, South Africa
[69] School of Physics and Astronomy, Cardiff University, Queens Buildings, The Parade, Cardiff, CF24 3AA, UK
[70] School of Physics and Astronomy, University of Nottingham, Nottingham NG7 2RD, UK
[71] Simon Fraser University, Department of Physics, 8888 University Drive, Burnaby BC, Canada
[72] Sorbonne Université-UPMC, UMR 7095, Institut d'Astrophysique de Paris, 98bis boulevard Arago, 75014 Paris, France
[73] Space Sciences Laboratory, University of California, Berkeley, CA 94720, USA
[74] Sub-Department of Astrophysics, University of Oxford, Keble Road, Oxford OX1 3RH, UK
[75] The Oskar Klein Centre for Cosmoparticle Physics, Department of Physics,Stockholm University, AlbaNova, 106 91 Stockholm, Sweden
[76] UPMC Univ Paris 06, UMR 7095, 98bis boulevard Arago, 75014 Paris, France
[77] Université de Toulouse, UPS-OMP, IRAP, 31028 Toulouse Cedex 4, France
[78] University of Granada, Departamento de Física Teórica y del Cosmos, Facultad de Ciencias, 18071 Granada, Spain
[79] Warsaw University Observatory, Aleje Ujazdowskie 4, 00-478 Warszawa, Poland

Appendix A: Stacking on *E*-mode peaks

Here we will discuss the new procedure of stacking on E-mode extrema. We remind readers that the full implementation and derivation of all relevant parameters are discussed in great detail in Appendix B of Komatsu et al. (2011), and a similar derivation is given in Contaldi (2015) for stacking on Q and U extrema. Here we simply explain the few details required to extend the formalism for stacking on E-modes.

Selecting the peaks of an underlying Gaussian field (like T or E) leads to a biased selection of that field. Such a bias is scale-dependent and has the form

$$\delta_{\rm pk}(\hat{\boldsymbol{n}}) = \left[b_\nu - b_\zeta \nabla^2\right] E(\hat{\boldsymbol{n}}). \tag{A.1}$$

The scale-dependent term (b_ζ) arises because peaks are defined by a vanishing first derivative and the sign of the second derivative (Desjacques 2008).

The bias parameters depend entirely on rms values of derivatives of the Gaussian field, σ_0, σ_1, and σ_2 (they also depend on special functions involved in translating a three-dimensional Gaussian random field to the two-dimensional case, as discussed in Bond & Efstathiou 1987). These are defined as

$$\sigma_j^2 \equiv \frac{1}{4\pi}\int {\rm d}\hat{\boldsymbol{n}} \left(\nabla^2\right)^j E^2(\hat{\boldsymbol{n}}) \tag{A.2}$$

$$= \frac{1}{4\pi}\sum_\ell (2\ell+1)[\ell(\ell+1)]^j (C_\ell^{EE} + N_\ell^{EE})(W_\ell^E)^2. \tag{A.3}$$

This is the only expression that contains the noise term N_ℓ^{EE}, which is why understanding the noise properties of the E-mode map is potentially considered to be a relevant systematic effect (see Sect. 6.1).

When we stack $Q_{\rm r}$ or $U_{\rm r}$ on the location of E-mode peaks we are explicitly computing the cross-correlation $\langle\delta_{\rm pk}(\hat{\boldsymbol{n}})Q_{\rm r}(\hat{\boldsymbol{n}}+\boldsymbol{\theta})\rangle$ or $\langle\delta_{\rm pk}(\hat{\boldsymbol{n}})U_{\rm r}(\hat{\boldsymbol{n}}+\boldsymbol{\theta})\rangle$. Recalling that both $Q_{\rm r}$ and $U_{\rm r}$ can be written in terms of E and B-mode contributions (Zaldarriaga & Seljak 1997; Kamionkowski et al. 1997) and rewriting Eq. (A.1) in the flat-sky approximation we arrive at[12]

$$\langle\delta_{\rm pk}(\hat{\boldsymbol{n}})Q_{\rm r}(\hat{\boldsymbol{n}}+\boldsymbol{\theta})\rangle = \int \frac{{\rm d}^2\boldsymbol{\ell}}{(2\pi)^2} W_\ell^E W_\ell^P (\bar{b}_\nu + \bar{b}_\zeta \ell^2)$$
$$\left\{C_\ell^{EE}\cos\left[2(\phi-\psi)\right] + C_\ell^{EB}\sin\left[2(\phi-\psi)\right]\right\} e^{i\boldsymbol{\ell}\cdot\boldsymbol{\theta}}, \tag{A.4}$$

$$\langle\delta_{\rm pk}(\hat{\boldsymbol{n}})U_{\rm r}(\hat{\boldsymbol{n}}+\boldsymbol{\theta})\rangle = \int \frac{{\rm d}^2\boldsymbol{\ell}}{(2\pi)^2} W_\ell^E W_\ell^P (\bar{b}_\nu + \bar{b}_\zeta \ell^2)$$
$$\left\{C_\ell^{EB}\cos\left[2(\phi-\psi)\right] - C_\ell^{EE}\sin\left[2(\phi-\psi)\right]\right\} e^{i\boldsymbol{\ell}\cdot\boldsymbol{\theta}}. \tag{A.5}$$

Here we have used the coordinate convention of Komatsu et al. (2011), thus $\boldsymbol{\ell} = (\ell\cos\psi, \ell\sin\psi)$, and $\boldsymbol{\theta} = (\theta\cos\phi, \theta\sin\phi)$. We can perform the internal integration over ψ using properties of Bessel functions to finally arrive at Eqs. (11)–(12), i.e.,

$$\langle\delta_{\rm pk}(\hat{\boldsymbol{n}})Q_{\rm r}(\hat{\boldsymbol{n}}+\boldsymbol{\theta})\rangle = -\int \frac{\ell{\rm d}\ell}{2\pi} W_\ell^T W_\ell^P \left(\bar{b}_\nu + \bar{b}_\zeta \ell^2\right)$$
$$C_\ell^{EE} J_2(\ell\theta), \tag{A.6}$$

$$\langle\delta_{\rm pk}(\hat{\boldsymbol{n}})U_{\rm r}(\hat{\boldsymbol{n}}+\boldsymbol{\theta})\rangle = -\int \frac{\ell{\rm d}\ell}{2\pi} W_\ell^T W_\ell^P \left(\bar{b}_\nu + \bar{b}_\zeta \ell^2\right)$$
$$C_\ell^{EB} J_2(\ell\theta). \tag{A.7}$$

These angular profiles could have been derived in a more heuristic way by realizing that an E-mode map has the same statistical properties as a temperature map, differing only in its power spectrum. Thus we could have gone from Eqs. (9)–(10) to Eqs. (11)–(12) by simply making the replacement $T \to E$.

[12] For brevity we henceforth drop the noise term in the expression for C_ℓ^{EE}.